https://doi.org/10.5194/egusphere-2026-3554
Preprint. Discussion started: 4 August 2026

Seasonal increase of the mixed-mode fracture toughness of faceted-crystal weak layers

Melin Walet[1], Jakob Schöttner[1], Valentin Adam[1,2], Florian Rheinschmidt[3], Philipp L. Rosendahl[2], Philipp Weißgraeber[3], Jürg Schweizer[1], and Alec van Herwijnen[1]

[1]WSL Institute for Snow and Avalanche Research SLF, Davos, Switzerland

[2]Institute of Structural Mechanics and Design, Technical University of Darmstadt, Darmstadt, Germany

[3]Chair of Lightweight Design, University of Rostock, Rostock, Germany

Correspondence: Melin Walet (melin.walet@slf.ch)

Abstract. Mixed-mode fracture toughness of natural snow weak layers has rarely been measured directly, yet it is a key parameter governing dry-snow slab avalanche release on inclined, snow-covered slopes. Most prior estimates relied on assumed elastic properties of slab and weak layer rather than direct measurements. Here, we present field-based fracture experiments investigating the seasonal evolution of the mixed-mode fracture toughness of a natural weak layer composed of faceted crystals. We introduce a novel method that combines digital image correlation of snow displacement fields with inverse modeling to derive effective elastic properties of both the weak layer and the overlying slab. These experimentally constrained elastic properties provided more robust estimates of weak layer fracture toughness than previously possible. Results show a clear increase in fracture toughness over the season from $0.29 \pm 0.042\ \mathrm{J\,m^{-2}}$ to $0.67 \pm 0.061\ \mathrm{J\,m^{-2}}$ in mode I and from $0.10 \pm 0.022\ \mathrm{J\,m^{-2}}$ to $1.0 \pm 0.1\ \mathrm{J\,m^{-2}}$ in mode II. The effective elastic modulus of the weak layer evolved from approximately $0.63 \pm 0.094\ \mathrm{MPa}$ at the beginning of the measurement period to $0.40 \pm 0.046\ \mathrm{MPa}$ later in the season, while slab elasticity increased from $16 \pm 1\ \mathrm{MPa}$ at the start to $41 \pm 2\ \mathrm{MPa}$. Furthermore, micro-computed tomography and manual snow profiles revealed that, although the weak layer density remained nearly constant, the specific surface area decreased and the mean local ice and pore thickness increased, as did the grain size. These findings suggest that the increases in both mode I and mode II fracture toughness are associated with grain size growth and growth of the bonds between the grains. The study further demonstrates that displacement-constrained inverse modeling provides robust snow elastic properties, improving fracture-mechanical estimates of avalanche release processes.

https://doi.org/10.5194/egusphere-2026-3554
Preprint. Discussion started: 4 August 2026

1 Introduction

Dry-snow slab avalanches, triggered by failures in weak layers within the snowpack, pose a danger in snow-covered mountainous environments. In Switzerland, on average, these avalanches are responsible for 22 fatalities each year (20-year mean) (WSL Institute for Snow and Avalanche Research SLF, 2025). Buried persistent weak layers consisting of faceted crystals, depth hoar, or surface hoar are particularly prone to failure initiation and crack propagation due to their fragile and porous microstructure, and are therefore often associated with slab avalanche release (e.g. Schweizer and Jamieson, 2001). Understanding the fracture processes in snowpacks consisting of weak layers is therefore critical for avalanche release prediction (e.g. van Herwijnen and Jamieson, 2007).

Fracture mechanics provides a useful framework for analyzing the processes leading to avalanche release (Schweizer et al., 2008). Within this framework, fracture toughness, which quantifies a material's resistance to crack propagation, is a key property for understanding weak layer fracture. Field-based experiments were developed to measure this property, most notably the propagation saw test (PST) (e.g. Gauthier and Jamieson, 2006). The PST has been widely used to investigate fracture processes in snow (e.g. van Herwijnen et al., 2010), and in combination with mechanical or numerical models, it can be used to estimate weak layer fracture toughness (e.g. Sigrist and Schweizer, 2007; Schweizer et al., 2011; van Herwijnen et al., 2016). However, most measurements have been performed in flat or low-angle terrain. In contrast, dry-snow slab avalanches typically release on slopes steeper than 30°, where mixed-mode fracture, combining mode I (opening) and mode II (in-plane shear), is dominant.

To better replicate these conditions, the mixed-mode fracture test (MMFT) was recently developed (Adam et al., 2024). The MMFT builds on the concept of the PST, but requires extracting the snow sample, placing it in a tilting device, applying additional loads, and then performing the test. This setup enhances and systematically controls shear contributions in the experiments, enabling the first empirical derivation of a mixed-mode interaction law for the fracture toughness of snow layers consisting of buried surface hoar. While this represented a significant step forward, the analysis relied on estimated elastic properties of the slab and weak layer. Because the computed critical energy release rates depend directly on these elastic parameters, these estimations introduced uncertainties in the computed critical energy release rates.

Measuring elastic properties in the field is not straightforward due to the fragile character of snow and the difficulty of measuring the instantaneous elastic response (e.g. Mellor, 1975; Gerling et al., 2017). Image-based methods offer a promising solution to independently estimate effective elastic properties in field experiments (van Herwijnen et al., 2010). The general approach consists of deriving snow deformation from video recordings and inferring elastic properties through comparison with theoretical predictions. Early work combined particle tracking with the anticrack model of Heierli and Zaiser (2008) to estimate the equivalent elastic modulus of the slab (van Herwijnen et al., 2016). More recently, digital image correlation (DIC) has enabled full-field displacement measurements (Bergfeld et al., 2021), while the layered first-order shear deformation theory beam model WEAC (Weißgraeber and Rosendahl, 2023), allows for simultaneous derivation of slab and weak layer elastic properties, accounting for snow stratigraphy. Using this approach, Bergfeld et al. (2023b) investigated the seasonal variation of elastic properties and specific fracture energy of layers of buried surface hoar, though still performing the experiments in the flat, where the mode II contributions are very small compared to the mode I contributions in the critical energy release rates.

https://doi.org/10.5194/egusphere-2026-3554
Preprint. Discussion started: 4 August 2026

Recent MMFT experiments (Adam et al., 2024) established the first compression–shear mixed-mode fracture-toughness interaction law for snow weak layers, but two key limitations remain. First, the available data are limited to buried surface hoar. Second, fracture toughness estimates rely on assumed elastic properties of the slab and weak layer. Consequently, it remains unclear whether the interaction law applies to other persistent weak layer types, such as faceted crystals, and how experimentally constrained elastic properties affect the inferred fracture toughness.

Here, we address these two limitations by combining mixed-mode fracture tests on a natural faceted-crystal weak layer with DIC-based inverse derivation of slab and weak layer elastic properties, using the WEAC model of Weißgraeber and Rosendahl (2023). Using three experimental campaigns over the course of a winter season, we derived the full mixed-mode interaction law for faceted crystals and investigated its seasonal evolution. We complemented our experiments by microstructural characterization using µCT scans.

2 Methods

We performed mixed-mode fracture tests (MMFTs) in the field and used video recordings of the experiments to inversely derive elastic properties of both the slab layers and the weak layer. These elastic properties were then used to calculate the critical energy release rates. The overall workflow is visualized in Figure 1 and detailed below.

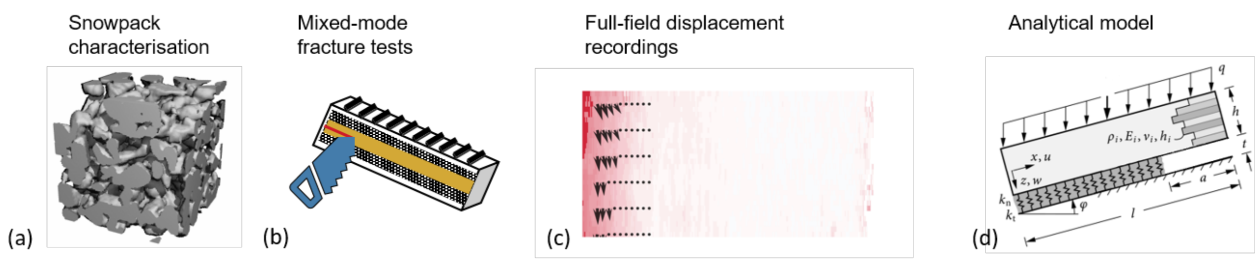

Figure 1. Workflow showing the different methodological steps. (a) First, we characterized the snowpack using snow profiles, SMP measurements, µCT scans and meteorological data. (b) Then, we performed field experiments including extracting, tilting and filming the sample. (c) We analysed video recordings of the full-field displacement, including post-processing and corrections. (d) Using an analytical model, we inversely derived the elastic properties to calculate the critical energy release rates and to establish mixed-mode interaction laws for the fracture toughness values.

2.1 Field site and snowpack characterisation

The experiments were conducted at the Steintälli field site next to the automatic weather station WAN7 (2442 m a.s.l., WGS84 46.807611 N, 9.787977 E) above Davos, Switzerland. We performed measurements in three series: Series I on 15 and 16 February 2023, Series II from 27 February to 3 March 2023, and Series III from 6 to 8 March 2023 (Figure 2a). The snowpack at the field site was characterized with manual snow profiles including density measurements following Fierz et al. (2009)

https://doi.org/10.5194/egusphere-2026-3554
Preprint. Discussion started: 4 August 2026

(Figure 2c). Snow micro-penetrometer (SMP) measurements (Schneebeli and Johnson, 1998) were used to investigate snow variability at the site: the transects hint towards relative snowpack homogeneity within the study site (Figure 2b). In addition, snow samples were extracted, including the weak layer, to derive microstructural parameters with micro-computed tomography (µCT; Schneebeli and Sokratov, 2004) in the cold laboratory at SLF. The first sample was transported to the cold lab in a styrofoam box and was prepared afterwards for the µCT holder. All other samples for µCT were placed in plastic bags filled with snow to avoid mechanical disturbance and temperature fluctuations and carefully transported to the cold laboratory at SLF in Davos. Samples that were damaged during transport were discarded.

We used µCT imaging (µCT90, Scanco Medical, Switzerland) to characterize the microstructure of the weak layer samples. 6 scans were performed at a voxel size of $(29.1\,\mu\mathrm{m})^3$, and 1 scan was performed at a voxel size of $(22.8\,\mu\mathrm{m})^3$. A cubic region of interest (ROI) was selected containing only the weak layer and, similar to the analysis performed and described in more detail by Schöttner et al. (2026), we derived the following microstructural properties. With Lucid Xamflow Desktop, we obtained density, specific surface area (SSA, a measure for the surface-to-volume ratio), correlation lengths and vertical anisotropy, indicating the preferred orientation of the structure. The open-source software ImageJ and the plugin BoneJ (e.g. Doube et al., 2010; Schindelin et al., 2012; Domander et al., 2021) were used to calculate the local ice thickness and local pore thickness, defined as the diameter of the largest sphere that fits in a structure. A plugin developed by Roque and Costa (2020) for ImageJ (Schneider et al., 2012) was used to calculate tortuosity, a measure for the complexity of paths through porous structures. Lastly, connectivity density (the amount of bonds per volume) was calculated following Odgaard and Gundersen (1993).

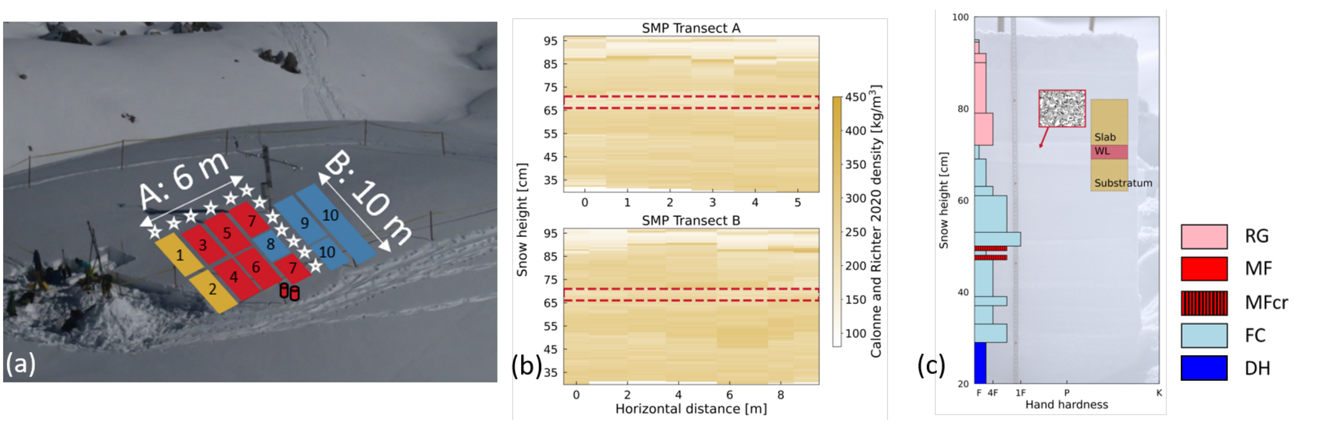

Figure 2. a) Bird's-eye view of the field site. The areas of the extracted samples are colored corresponding to their measurement series (Series I: yellow, Series II: red, Series III: blue) and numbered per measurement day. The cylinders in the lower right side mark the location of the samples for the µCT scans. The white stars (⋆) mark the locations of the SMP intersects, with intersect A being 6 m long and intersect B being 10 m long. b) SMP measurements of transect A (top) and transect B (bottom) in the field site. c) Snow profile taken on 14 February 2023, with a 2D µCT image of the weak layer. Grain types are colored following Fierz et al. (2009).

https://doi.org/10.5194/egusphere-2026-3554
Preprint. Discussion started: 4 August 2026

2.2 Mixed-mode fracture test

We applied the mixed-mode fracture test (MMFT) as introduced by Adam et al. (2024) (Figure 3e). For the MMFT, we used a metal sledge to extract a snow sample of approximately $1\ \mathrm{m} \times 0.3\ \mathrm{m}$ that contained the weak layer we were testing (Figure 3f). The sledge was inserted into the snowpack about $10\ \mathrm{cm}$ below the weak layer (Figure 3a). The sidewalls were then cut vertically with a snow saw, and the sample was placed on a base plate in the tilting device (Adam et al., 2024). The base plate included nails that pierced the substratum to prevent sliding. The slab was then trimmed to $13\ \mathrm{cm}$, and stair-step notches were cut in the top of the slab to position the weights. For the DIC analysis, one side of the snow sample was speckled with black ink, and the sample was tilted to the desired incline before placing the weights (12 steel cylinders with steel rods in them, with a total mass of $36 \pm 2\ \mathrm{kg}$, taking into account variations in the exact mass of the different rods used during the experiments) on top of the slab (Figure 3d). The incline was measured along the weak layer, and the slab height was measured from the weak layer to the top of the slab. The weak layer was cut into using a snow saw. Once the critical cut length was reached, the crack propagated. The experiments were recorded with a Sony camera (1920×1080 px at 50 frames per second) following Bergfeld et al. (2021). The camera was rotated such that its view was always aligned with the length of the sample. Slab densities were measured with a density cutter (diameter $3\ \mathrm{cm}$, volume $100\ \mathrm{cm}^3$) at three positions over the height of the slab (top, middle, bottom) and weak layer; slab temperatures were measured immediately after each test.

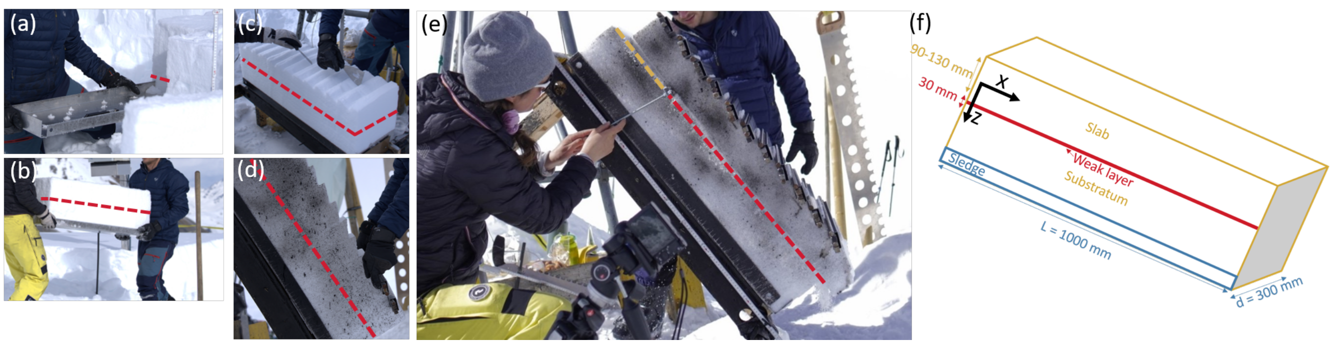

Figure 3. a) and b) Extraction of the sample using the sledge, with the weak layer highlighted by the red dashed line. c) Preparation of the sample by creating stair-step notches in the slab. d) Close-up of the stair-step notches in the slab and the weights that are placed in these notches. e) MMFT setup, including the weights on top of the slab and a camera in front of the setup. Captured is the moment just after the critical cut length was reached (indicated by the yellow dotted line), when the crack propagates through the weak layer and the slab has already started to slide down. f) Schematic overview of the MMFT setup: the weak layer is highlighted in red. Below the weak layer is the substratum, placed on top of the aluminum sledge.

2.2.1 Video analysis and displacement signals

The video recordings of each experiment were used for three purposes. First, they provided a verification tool to identify and discard failed experiments, such as cases where the saw cut was out of the weak layer, the sample lifted from the sledge, or

https://doi.org/10.5194/egusphere-2026-3554
Preprint. Discussion started: 4 August 2026

premature sliding occurred. Second, the videos allowed us to determine the critical cut length by identifying the frame in which self-sustained crack propagation initiated. Third, the recordings were analyzed using digital image correlation (DIC) to obtain two-dimensional displacement fields during sawing.

To quantify displacement fields during the fracture experiments, we used the open-source DICe software (Turner et al., 2015) in subset-based full-field mode with feature-matching initialization. The following parameters were chosen after preliminary sensitivity tests: subset size (of the region used for correlation) = 21 pixels, step size (the distance between neighbouring regions) = 5 pixels, and a SSSig threshold (a quality filter) = 30. For spatial calibration, a ruler placed in the field of view allowed conversion from pixels to physical displacements, with a typical scaling factor of $1.7\,\mathrm{px/mm}$. The displacement fields were extracted for both vertical (w) and horizontal (u) directions relative to the slab coordinate system, with the z-axis oriented downslope along the slab height and the x-axis aligned parallel to the slab length and the origin positioned at the leftmost edge of the sample at half of the slab height.

The DIC procedure yielded raw displacement fields for each frame up to and including the frame where the critical cut length was reached. The raw displacement fields contained systematic noise and artefacts that had to be corrected. These artefacts were mainly due to static offsets, rigid-body motion of the sledge, and vertical drifts across the slab. To address this, we defined two regions of interest in the images, namely the snow block and the sledge at the bottom of the snow sample. We then applied the following corrections:

1. **Static noise removal:** The displacement of the initial undeformed frames was subtracted from the displacement in all subsequent frames to eliminate static offsets and set the reference state to zero.

2. **Correction for sledge motion:** A rigid-body fit was applied to the displacement of the sledge region in each frame. The resulting motion was subtracted from the entire field, removing the apparent tilt caused by the movement of the experimental setup.

3. **Correction for vertical offset:** The average displacement of the slab on the far edge of the sample was constrained to zero at each time step. This stabilized the reference frame and eliminated vertical drifts.

These three corrections provided consistent displacement fields, which were used in all subsequent analyses. Note that we also tested additional filtering approaches (Savitzky–Golay smoothing, scikit-image restoration, and non-local means filtering) to evaluate their potential effect on the displacement fields. Since these filters did not improve results and, in some cases, distorted the fields, they were not included in the final workflow.

2.2.2 Derivation of effective elastic properties

The effective elastic properties of both the slab and the weak layer were inversely derived by matching the measured displacements from DIC with the predictions from the WEAC layered beam model (Weißgraeber and Rosendahl, 2023). The model required as input the weak layer Poisson's ratio, the geometry of the slab, the slab density profile as obtained from three density cutter measurements, weak layer thickness and cut length. The Poisson's ratio of the weak layer ν_{wl} was assumed to be 0.25,

https://doi.org/10.5194/egusphere-2026-3554
Preprint. Discussion started: 4 August 2026

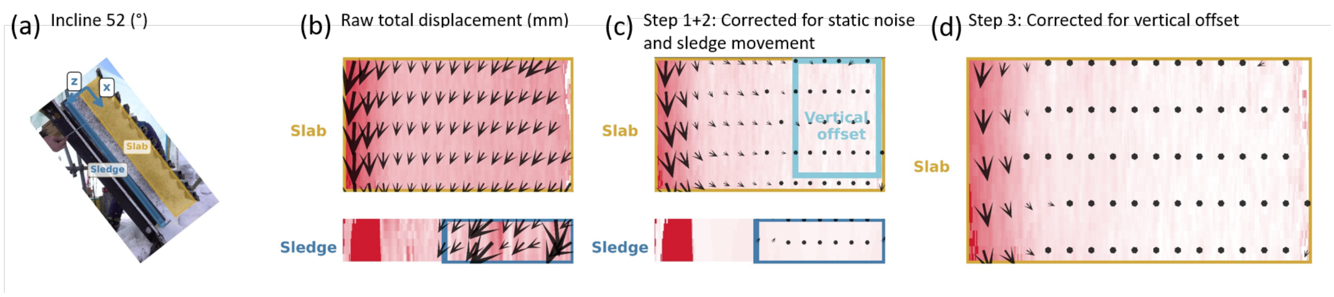

Figure 4. From video frame to post-processed displacement signal: a) Example experiment with an incline of 52°. The slab is highlighted in yellow and the sledge in blue. The coordinate system is indicated by the light blue arrows. (b) Total displacement field of the slab (yellow frame) and below of the sledge (blue frame) at a specific moment during cutting. Sledge displacements are artefacts from the motion of the setup, and are hence filtered out in the postprocessing. (c) Step 1+2: the displacement is corrected for static noise and linear sledge movement. The light blue "Filter area" indicates the area for the third post-processing step. (d) Step 3: Correction for vertical offset. Red colors in the color plots indicate a positive, downward displacement.

as a sensitivity analysis of Adam et al. (2024) showed it had negligible influence on the results. Moreover, the model contained two free parameters: i) the weak layer elastic modulus and ii) the density exponent γ governing the scaling of slab elastic modulus with density following Gerling et al. (2017):

$$E_i = E_0 \left(\frac{\rho_i}{\rho_{ice}} \right)^{\gamma}, \tag{1}$$

where $E_0 = 6.5 \times 10^3$ MPa, $\rho_{ice} = 917\,\mathrm{kg\,m^{-3}}$ and ρ_i is the density per layer within the slab.

After post-processing the displacement signals (Section 2.2.1), we defined a region of interest (ROI) within the slab for model fitting. For vertical displacements, a larger ROI was selected, including the area near the saw tip, even if some noise was present. For horizontal displacements, a smaller ROI was chosen to exclude the most critical (but noisy) region, since horizontal displacements were small in magnitude and more affected by DIC artefacts. As displacements for short cut lengths at the start of the experiment were generally small, we only used frames between 75–90% of the critical cut length. This captured the deformation immediately prior to crack propagation, while using multiple frames reduced the influence of single-frame noise. As some experiments were not recorded on video, all experiments with video recordings of a measurement series were fitted simultaneously under the assumption that slab and weak layer properties remained constant within one measurement series. The ensemble-based optimization results were then used for all experiments in the series, also for those without video recordings. Pooling the experiments improved robustness and reduced the influence of outliers.

The optimization was implemented in Python (ipython 8.12.3, matplotlib 3.9.1.post1, numpy 2.0.1, pandas 2.2.3, scipy 1.14.0, weac 2.6.4) using the `scipy.optimize.leastsquares` routine with tolerances of 10^{-4}. The objective function minimized the weighted sum of squared residuals between measured and modeled displacements:

$$\hat{\theta} = \arg\min_{\theta} \sum_{i=1}^{n} \sum_{k=1}^{k_{i,j}} \frac{1}{N_i} \frac{1}{A_{i,j}} \left[0.75 \left(w_{k,\mathrm{exp}} - w_{k,\mathrm{model}}(\theta) \right)^2 + 0.25 \left(u_{k,\mathrm{exp}} - u_{k,\mathrm{model}}(\theta) \right)^2 \right], \tag{2}$$

https://doi.org/10.5194/egusphere-2026-3554
Preprint. Discussion started: 4 August 2026

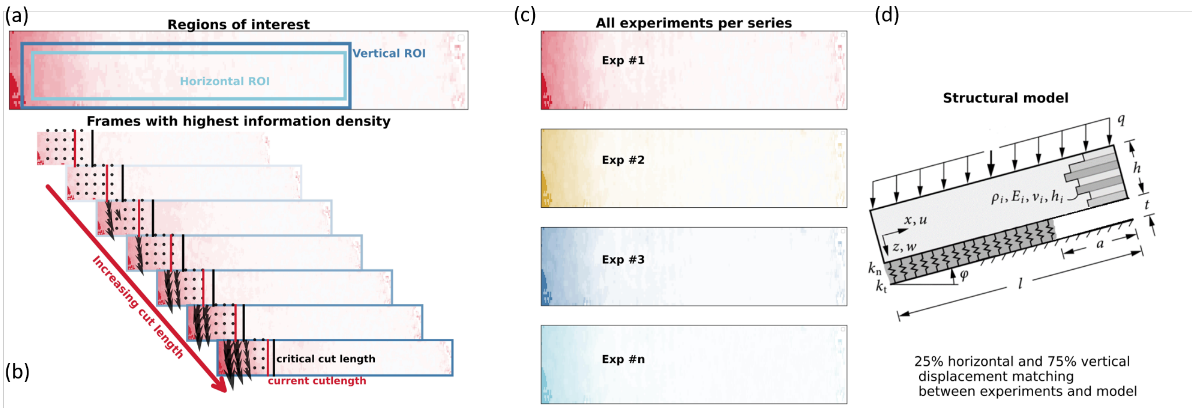

Figure 5. Schematic overview of the elastic properties derivation. a): Regions of interest (ROIs) within the slab for the vertical and the horizontal displacements. b): Time interval of 75–90% of the critical cut length. This spatial and temporal selection is done for each experiment individually. c) All experiments within one measurement series were used, with vertical and horizontal displacements weighted by 75% and 25%, respectively. Displacements were normalised by ROI size and the number of frames per experiment, before being matched with d): the WEAC model (reproduced from Weißgraeber and Rosendahl (2023)).

where θ is the vector of model parameters being optimized and $\hat{\theta}$ is the optimal parameter estimate obtained by minimizing the cost function. For each experiment, frames between 75–90 % of the critical cut length were included. The outer sum ran over experiments $i = 1, \ldots, n$, with N_i the number of frames used as the normalization factor for experiment i to ensure experiments with more frames did not dominate the optimization. The innermost sum ran over measurement points $k = 1, \ldots, k_{i,j}$ within each frame. Each frame was normalized by its ROI size $A_{i,j}$ so that frames with different numbers of measurement points contributed equally. $w_{k,\text{exp}}$ and $u_{k,\text{exp}}$ are the measured vertical and horizontal displacements, while $w_{k,\text{model}}(\theta)$ and $u_{k,\text{model}}(\theta)$ are the corresponding model predictions for parameter set θ. The optimization routine ran over variations of the model and experiment displacements (Monte Carlo, n=100) to obtain the parameters (E_wl and γ). Vertical displacements were given 75% weight because they are typically larger and less affected by artefacts, while horizontal displacements were given 25% weight. The residuals were normalized by the number of frames per experiment and by the size of the vertical and horizontal ROIs, to ensure all experiments were weighted equally, also experiments with a small ROI and/or only a few frames. The optimization workflow is visualised in Figure 5. The median values of the Monte Carlo optimization outcomes were used as parameter values, and the confidence intervals are based on twice the median absolute deviation of the parameter distribution. Parameter bounds were set to $0.01 < E_\text{wl} < 30$ MPa and $2 < \gamma < 8$, with initial values E_wl = 0.2 MPa and γ = 4.4.

We consider the following uncertainties. First, we use the standard deviation of the displacement before sawing as uncertainty for the displacements measured via DIC. Second, we define measurement uncertainties in the physical input for the model, which we propagate via Monte Carlo random sampling (n=100) to the model displacement: cut length ($\pm 10\,\text{mm}$), layer density ($\pm 10\,\%$), layer thickness ($\pm 5\,\%$), incline ($\pm 2°$) and surface load ($\pm 2.5\,\%$). Lastly, we define the uncertainties in the obtained parameters E_wl and γ as the median absolute deviation of the parameter contribution.

https://doi.org/10.5194/egusphere-2026-3554
Preprint. Discussion started: 4 August 2026

From the identified properties, we also calculated the slab bending stiffness D_{11}, which controls the bending resistance of the layered slab and thereby affects crack-tip loading:

$$D_{11} = \frac{1}{3}\sum_{k=1}^{N} \frac{E_k}{(1-\nu_k^2)} \left(z_k^3 - z_{k-1}^3\right), \tag{3}$$

where $\frac{E}{(1-\nu^2)}$ is the transformed reduced stiffness of ply (layer within the slab) k, z_k and z_{k-1} are distances from the mid-plane to the top and bottom of ply k, and N is the number of plies.

With the identified elastic properties, the model of Weißgraeber and Rosendahl (2023) was then used to compute the critical energy release rates in mode I ($\mathcal{G}_\mathrm{I}$) and mode II ($\mathcal{G}_\mathrm{II}$) for each experiment. The required inputs included the tilt angle, the critical cut length, the optimized weak layer modulus E_wl, the density exponent γ, slab layer densities, geometric parameters (slab length and height), and the applied surface loads. Finally, to obtain the mixed-mode fracture toughness, we fitted the failure data from each measurement series using orthogonal distance regression (ODR, Boggs et al. (1987)) and the following mixed-mode interaction law:

$$\left(\frac{\mathcal{G}_\mathrm{I}}{\mathcal{G}_\mathrm{Ic}}\right)^{1/n} + \left(\frac{\mathcal{G}_\mathrm{II}}{\mathcal{G}_\mathrm{IIc}}\right)^{1/m} = 1, \tag{4}$$

where $\mathcal{G}_\mathrm{Ic}$ and $\mathcal{G}_\mathrm{IIc}$ denote the critical mode I and mode II energy release rates, respectively. We adopted this power law, recently introduced for mixed-mode anticracks in snow weak layers by Adam et al. (2024), as this form permits mode I and mode II to have different critical energy release rates and describes a smooth, closed mixed-mode fracture envelope. The interaction exponents n and m determine the degree of coupling between the two modes, with $n, m \to 0$ corresponding to independent failure modes and $n, m = 1$ representing strong interaction. In this study, we fitted one pair of interaction exponents, n and m, shared across all measurement series, while allowing $\mathcal{G}_\mathrm{Ic}$ and $\mathcal{G}_\mathrm{IIc}$ to vary between series. We filtered out the two data points with $\mathcal{G}_\mathrm{II}$ lower than $0.01\,\mathrm{J\,m^{-2}}$ to avoid overfitting in the region of almost pure mode I values.

https://doi.org/10.5194/egusphere-2026-3554
Preprint. Discussion started: 4 August 2026

3 Results

A total of 118 experiments were performed on a weak layer of faceted crystals over a three-week period. Although the experiments were performed on 10 different days, these were grouped into three measurement series consisting of consecutive days with minimal weather variations (see meteorological data in Appendix Figures A6, A7 and A8 for details): (I) 15 and 16 February 2023 (20 experiments), (II) from 27 February to 3 March (64 experiments), and (III) from 6 to 8 March (34 experiments). A total of 77 experiments were filmed and subsequently analyzed to identify the critical cut length. 74 of these were analyzed using digital image correlation. Of these, 41 videos were of sufficient quality for deriving the elastic properties using series optimization. Table 1 provides a complete overview of the number of experiments used.

Table 1. Overview of the number of experiments per series, used or discarded in various postprocessing steps.

	Series I	Series II	Series III	Total
Total number of experiments performed	20	64	34	118
Excluded from any further analysis	2	0	0	2
Filmed experiments	14	47	16	77
Used for video cut length determination	14	47	16	77
Used for DIC displacement fields	11	47	16	74
Used for inverse elastic properties derivation (series optimization)	9	24	8	41
Assigned series-specific elastic properties and calculated fracture toughness	13	64	34	111
Data points used for fracture-envelope fitting after filtering	12	63	34	109

3.1 Critical cut length

Our results indicated a clear increase in the cut length with increasing tilt angle for downslope cuts (positive inclines in Figure 6a). On the contrary, for upslope cuts (negative inclines), the cut length only showed a slight increase with increasing incline. The 77 video recordings were used to more accurately identify the critical cut length. On average, these video-derived values were slightly lower than the cut length measured manually in the field (Figure 6b).

3.2 Elastic properties of weak layer and slab

Performing the experiments under different inclines and cut directions resulted in markedly different slab displacement fields (Figure 7). For an upslope cut at $64 \pm 2^{\circ}$ the displacement field was mostly characterized by bending of the slab and large displacements at the cutting side of the slab and a relatively large horizontal component due to gravity in this steep configuration (Figure 7a-c). In the flat configuration (Figure 7d-f), the horizontal displacement component and the total displacement itself were much smaller, which is expected due to the shorter cut length compared to a steep configuration. For a downslope cut at $59 \pm 2^{\circ}$, the displacement field included a horizontal component opposite to the cutting direction (Figure 7g-h). In the cases

https://doi.org/10.5194/egusphere-2026-3554
Preprint. Discussion started: 4 August 2026

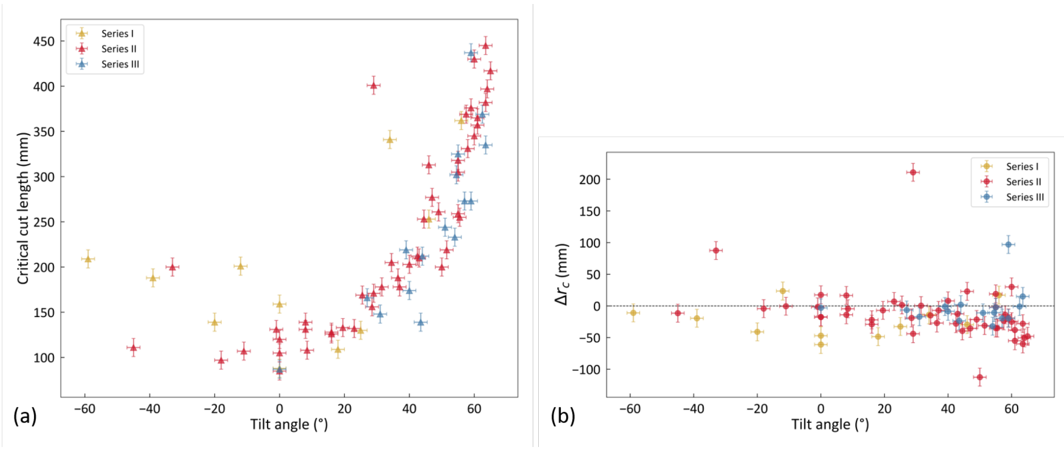

Figure 6. a) The critical cut lengths identified by video recordings as a function of tilt angle. b) The difference Δr_c between critical cut lengths identified by video and manually recorded critical cut lengths.

shown in Figure 7, the displayed cut lengths were similar, close to the critical cut length. Geometrical effects in the downslope case caused a small downward displacement at the uncut side of the slab as the slab slightly tilted outward due to gravity. In contrast, in the upslope case, there was some upward displacement at the uncut side, again due to the geometry.

The match between the model and the series of experiment displacements (following the method as described in Section 2.2.2) provided us with the effective elastic modulus of the weak layer (E_{wl}) and the density parametrisation exponent γ. The results of the series optimization were between 0.40 ± 0.046 MPa and 0.66 ± 0.037 MPa for the weak layer effective elastic modulus (summarized in Table 2 and visualized in Figure 8). Series I and II yielded similar values, whereas Series III showed a lower value. The identified γ values resulted in relatively wide ranges for the individual elastic modulus per sample within each series, due to the individual density measurements. The mean elastic modulus per series increased from Series I to Series II and Series III. The uncertainties in the slab elastic moduli were calculated using the uncertainty of the identified γ values. In Table 2, we noted the min-max range of the individual elastic moduli and the mean value of each measurement series. In the appendix, the detailed results of the Monte Carlo sampling are available (Figure A2).

The bending stiffness D_{11} increased with the power of three of the total slab thickness (Figure 9a). Measurement series III had a lower total slab thickness and a correspondingly lower bending stiffness than Series I and II. The density also impacted the bending stiffness (Figure 9b), with the change in bending stiffness between Series II and Series III mainly being caused by the change in slab thickness, whereas the changes in bending stiffness between Series I to II were mainly caused by the change in density.

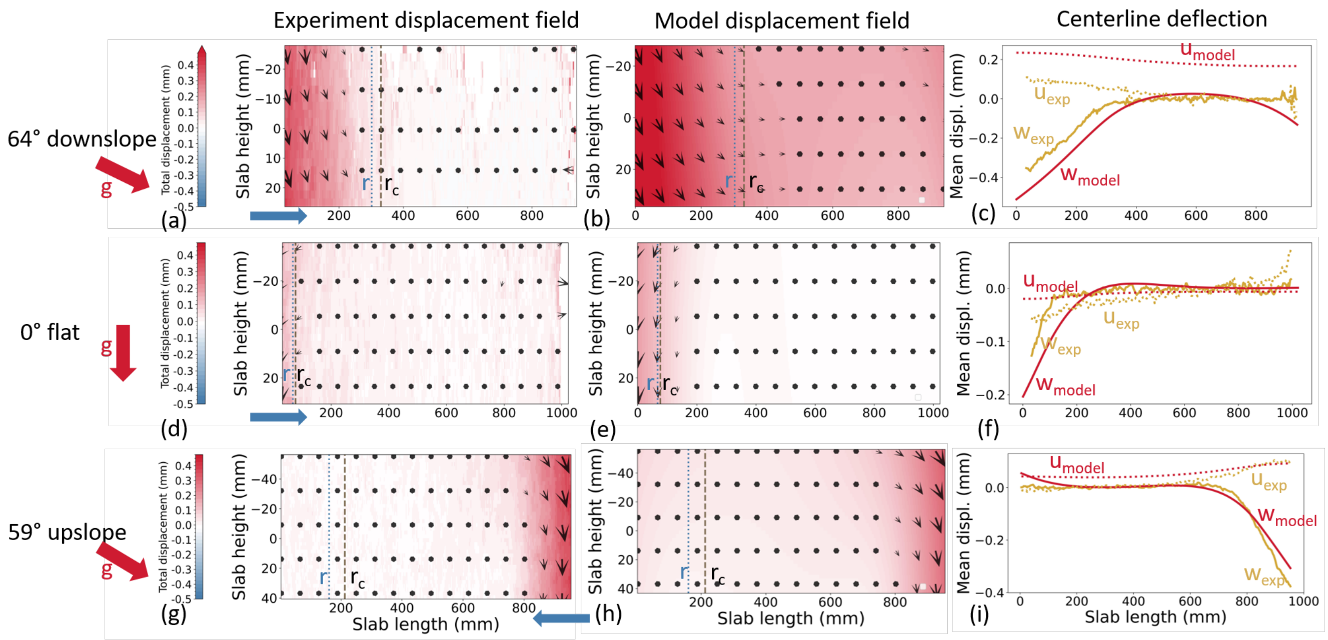

Figure 7. Examples of displacement field of (a) a steep downslope (64°), (d) a flat (0°), and (g) a steep upslope (−59°) fracture test. In all subfigures, the left figure shows the total displacement of the slab as measured in the experiment, at a certain cut length indicated by the blue dotted vertical line. The middle figure shows the total displacement of the slab by the model, using the identified elastic properties as input (the "perfect" match for the corresponding series). In the figure on the right, the mean slab displacements per x-location (averaged over the slab height) at the same moment in time are depicted. Depicted are the experiment displacement and the model displacement using the identified elastic properties. Displacements are in millimeters. The downslope and flat tests were cut from left to right, and the upslope test from right to left.

3.3 Fracture data

3.3.1 Seasonal development of critical energy release rates

Using the derived elastic properties, we calculated the critical energy release rates of the weak layer in mode I and in mode II, for the three measurement series (Figure 10). We observed an increase in total weak layer critical energy release rates throughout the season (Figure 11a). The mode II fraction reached high values for high inclines, but never reached 100 % of the total critical energy release rates (Figure 11b).

3.3.2 Mixed-mode interaction law for fracture toughness

We fitted the fracture data as described in the Methods section by Equation 4. For the fracture data using the derived elastic properties ("Series optimization") and the video cut length when available, we obtained a power law per measurement series

https://doi.org/10.5194/egusphere-2026-3554
Preprint. Discussion started: 4 August 2026

Table 2. Elastic properties of the weak layer and the slab. The column N_{exp} shows the number of experiments per day, with in brackets the number of usable/filtered video recordings. The three different measurement series are separated by the horizontal lines. Since the slab elasticities were calculated using the γ value and the three slab layer densities per experiment, we obtained three values per experiment within each series. For simplicity, we then calculated the mean elastic modulus per experiment ($E_{\text{slab\_mean}}$) by taking the average of the densities of the three layers per experiment. We display here the minimum and maximum of these mean densities within each series, as well as the mean value per series.

Series	Date	N_{exp} (N_{videos})	E_{wl} [MPa]	γ	$E_{\text{slab\_mean}}$ [MPa]		
					Min	Max	Mean
I	15 Feb 2023	8 (3)	0.63 ± 0.094	4.97 ± 0.18	11.4 ± 2.62	20.68 ± 4.27	15.8 ± 0.95
	16 Feb 2023	10 (6)					
II	27 Feb 2023	2 (0)	0.66 ± 0.037	4.65 ± 0.11	27.9 ± 3.60	54.6 ± 6.13	40.6 ± 0.60
	28 Feb 2023	11 (5)					
	1 March 2023	15 (6)					
	2 March 2023	21 (5)					
	3 March 2023	15 (8)					
III	6 Mar 2023	9 (0)	0.40 ± 0.046	4.61 ± 0.24	26.0 ± 7.41	66.2 ± 15.72	40.6 ± 1.84
	7 March 2023	14 (7)					
	8 March 2023	11 (1)					

(Figure 12) with increasing values for both mode I and mode II critical energy release rates throughout the season. A summary of the obtained fit values for the critical energy release rates $\mathcal{G}_{\text{Ic}}$ and $\mathcal{G}_{\text{IIc}}$ is presented in Table 3.

3.4 Influence of microstructure on fracture behavior

We collected a total of 7 samples for µCT scanning from the test site: one on 14 February (at the start of measurement series I), two on 28 February (at the start of measurement series II), two on 2 March (at the second to last day of measurement series II) and two on 8 March 2023 (on the last day of measurement series III). These CT scans included the weak layer. See Figure A3 in the Appendix for the 2D and 3D reconstructed images. Here, we focus on a selection of key parameters that are most relevant to the microstructural evolution in the weak layer. Notably, the weak layer density remained relatively constant, whilst the SSA decreased over time (Figure 13a). The mean local thickness in both pore space and ice increased (Figure 13b). This indicates growth of both snow grain size as well as the pore space between the grains. Additionally, manual snow profiles showed an increase in grain size from 0.5-0.75 mm to 1.25-1.5 mm.

https://doi.org/10.5194/egusphere-2026-3554
Preprint. Discussion started: 4 August 2026

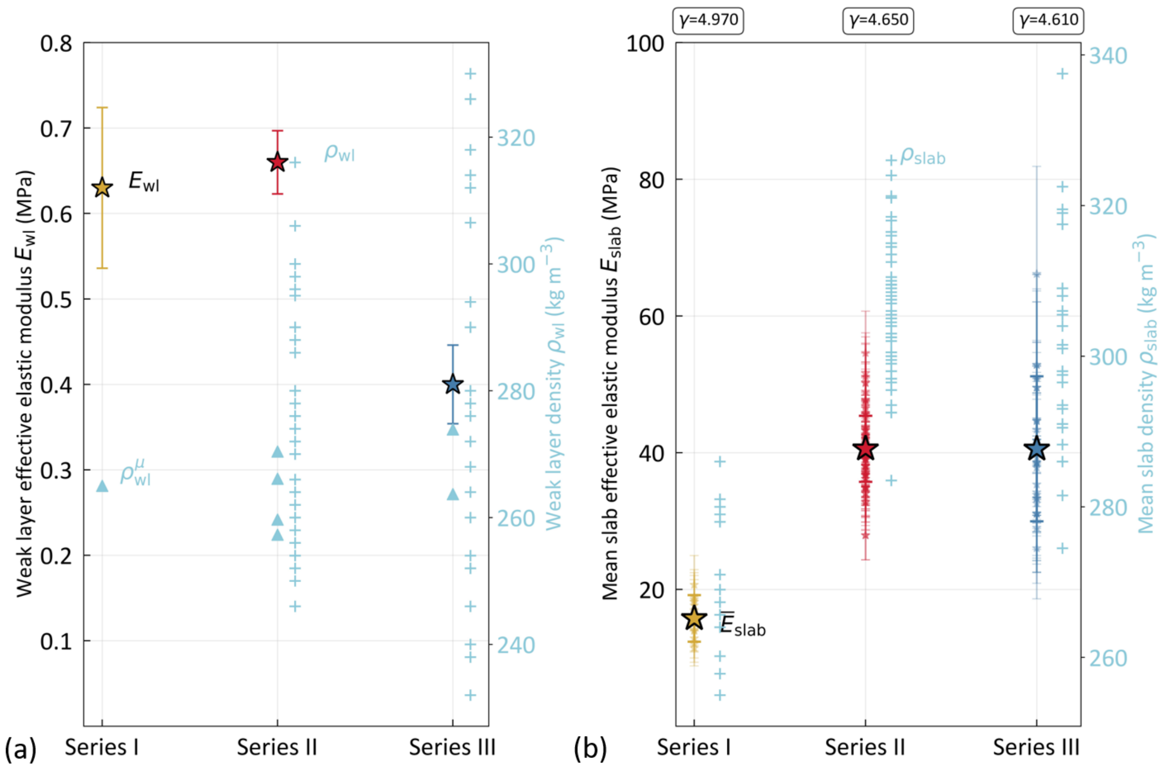

Figure 8. a) The effective elastic modulus of the weak layer per measurement series (stars). In light blue are the weak layer densities, measured in the field using the density cutter ("plus" signs) and obtained from the μCT scanner (triangles). b) The mean effective elastic modulus of the slab for each sample (small stars), calculated by the identified density parametrization exponent γ and Bergfeld's density parametrization. The large stars with black edges show the mean effective elastic modulus for the entire measurement series. The light blue plus signs are the mean slab densities per sample, based on the density cutter measurements.

4 Discussion

This study presents a complete mixed-mode fracture envelope for faceted crystals, based on effective elastic properties derived from displacement fields rather than assumed values. By combining MMFT experiments with DIC-based inverse derivation and series optimization, we reduced parameter uncertainty and extended elastic property estimates to tests without video data (Figure 5). Our results indicate that the weak layer elastic modulus ranged from 0.40 ± 0.05 MPa in Series III to 0.66 ± 0.04 MPa in Series II (Table 2), that $\mathcal{G}_{IIc}$ was slightly larger than $\mathcal{G}_{Ic}$ for Series II and III (Figure 12) but smaller for Series I, and that both critical energy release rates increased over the course of the season (Table 3, Figure 10). Microstructural observations (Figure 13) were qualitatively consistent with the seasonal increase of the fracture toughness.

https://doi.org/10.5194/egusphere-2026-3554
Preprint. Discussion started: 4 August 2026

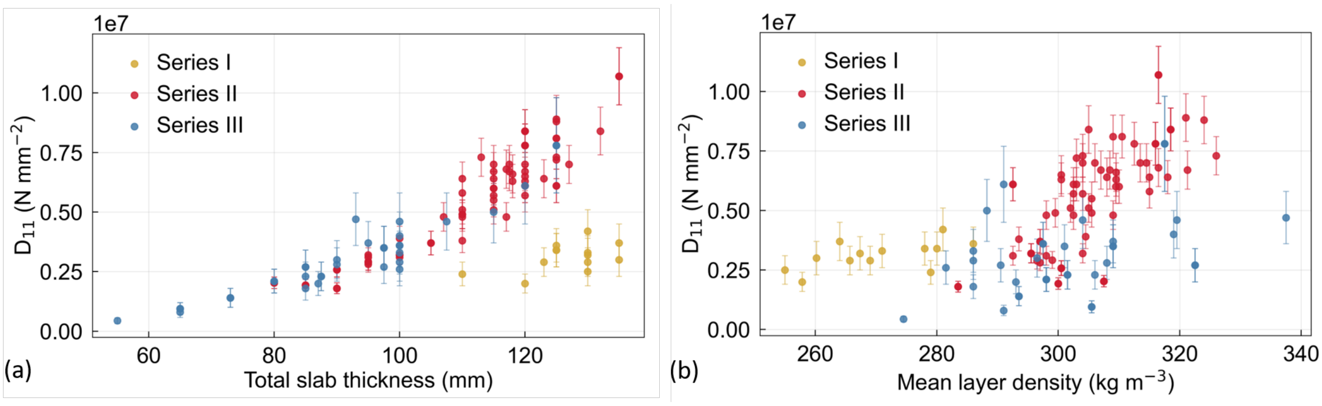

Figure 9. a) Bending stiffness D_{11} against total slab thickness. The three measurement series are distinguished with the colors yellow, red and blue. b) Bending stiffness against the mean slab density.

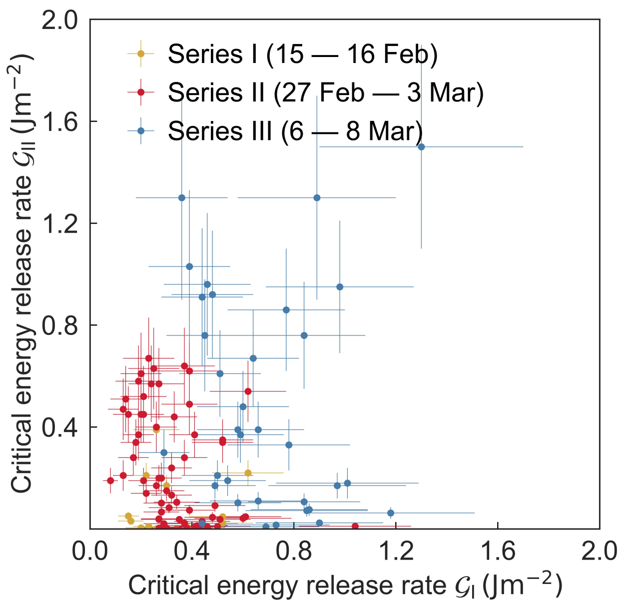

Figure 10. The critical energy release rates in mode II versus mode I. The colors indicate the three different measurement series: Series I has 13 data points, Series II has 64 data points and Series III has 34 data points.

https://doi.org/10.5194/egusphere-2026-3554
Preprint. Discussion started: 4 August 2026

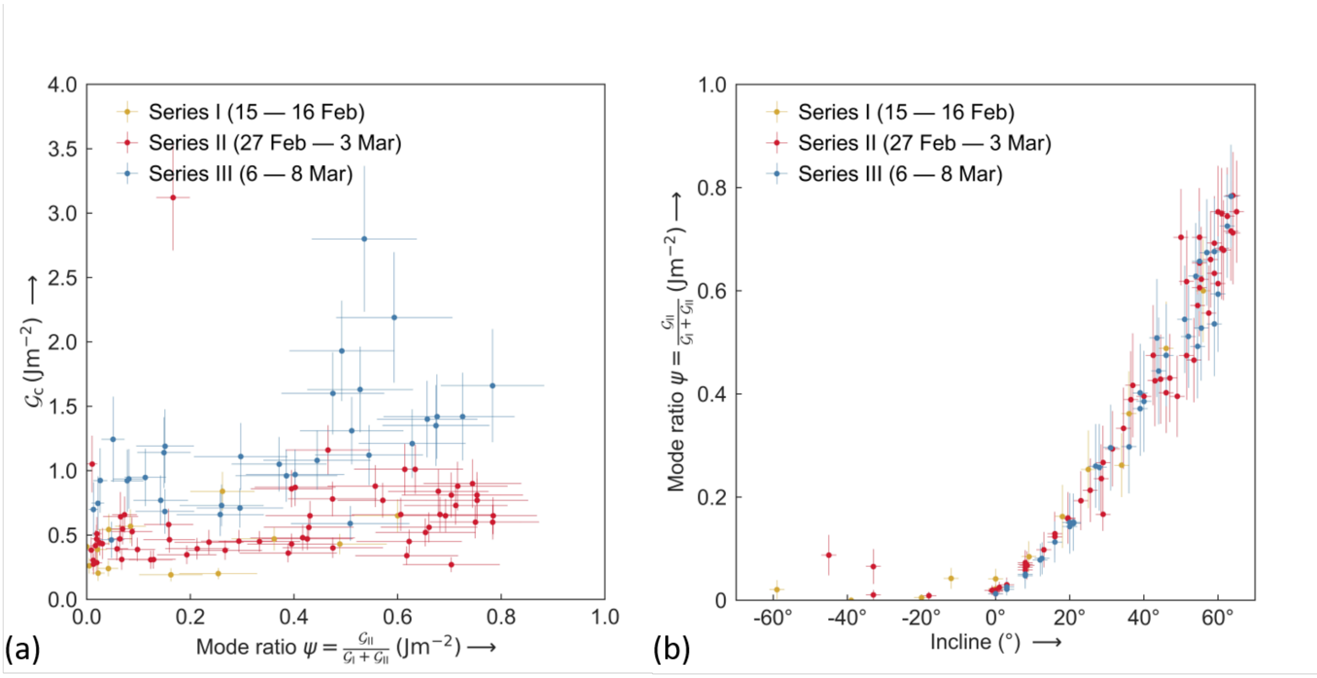

Figure 11. a) Total critical energy release rates as a function of mode ratio ψ (mode II fraction). b) Mode ratio showing the mode II contribution in the total critical energy release rate as a function of incline.

Table 3. Fitting parameters n = 0.178 and m = 0.277 for the mixed mode interaction law $\left(\frac{\mathcal{G}_{I}}{\mathcal{G}_{Ic}}\right)^{1/n} + \left(\frac{\mathcal{G}_{II}}{\mathcal{G}_{IIc}}\right)^{1/m} = 1$ for the fracture data, filtered on $\mathcal{G}_{II} > 0.01\ \mathrm{J\,m^{-2}}$.

	$\mathcal{G}_{Ic}$	$\mathcal{G}_{IIc}$
Series 1 (N=12)	0.29 ± 0.042	0.10 ± 0.022
Series 2 (N=63)	0.36 ± 0.024	0.34 ± 0.034
Series 3 (N=34)	0.67 ± 0.061	1.0 ± 0.18
n	0.178	
m	0.277	
Chi squared	3.51	
p-value	< 0.001	
R-squared	0.222	

https://doi.org/10.5194/egusphere-2026-3554
Preprint. Discussion started: 4 August 2026

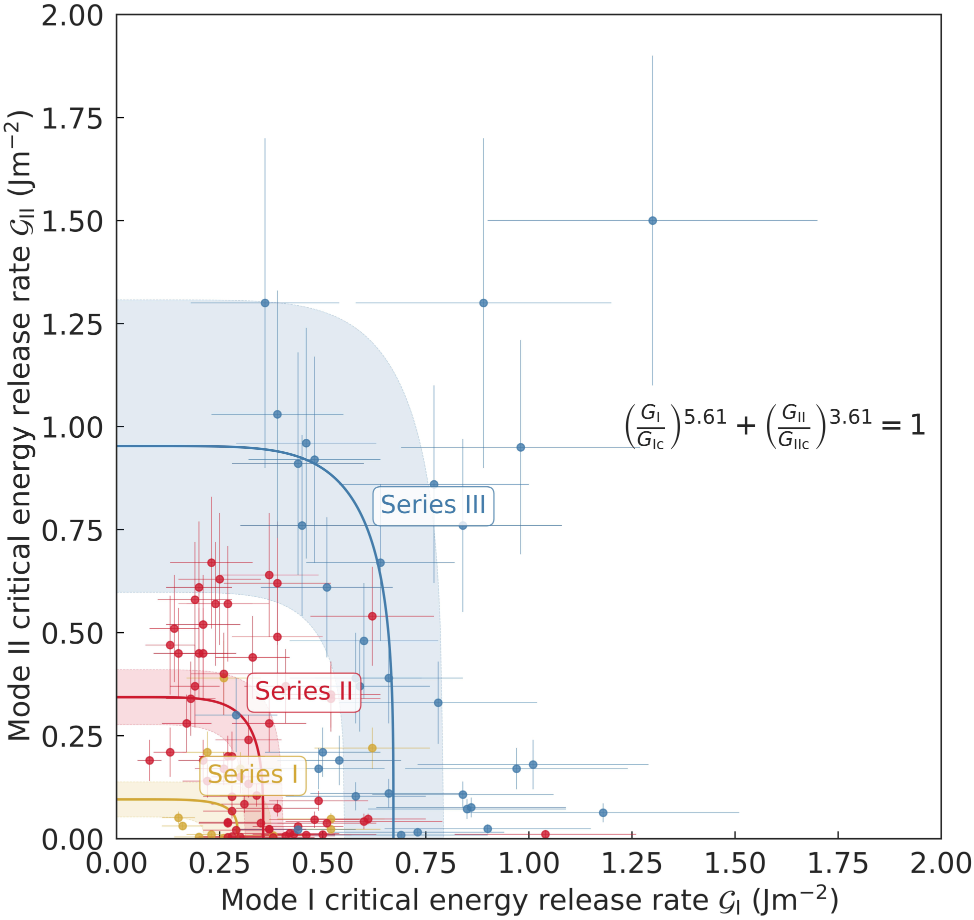

Figure 12. Interaction law $(\mathcal{G}_I/\mathcal{G}_{Ic})^{\frac{1}{n}} + (\mathcal{G}_{II}/\mathcal{G}_{IIc})^{\frac{1}{m}} = 1$ with n = 0.178 and m = 0.277 (1/n = 5.61, 1/m = 3.61) for each of the three measurement series. The data were filtered to have $\mathcal{G}_{II} > 0.01$, thus for Series I, 12 data points were used, for Series II, 63 data points, and for Series III, 34 data points.

https://doi.org/10.5194/egusphere-2026-3554
Preprint. Discussion started: 4 August 2026

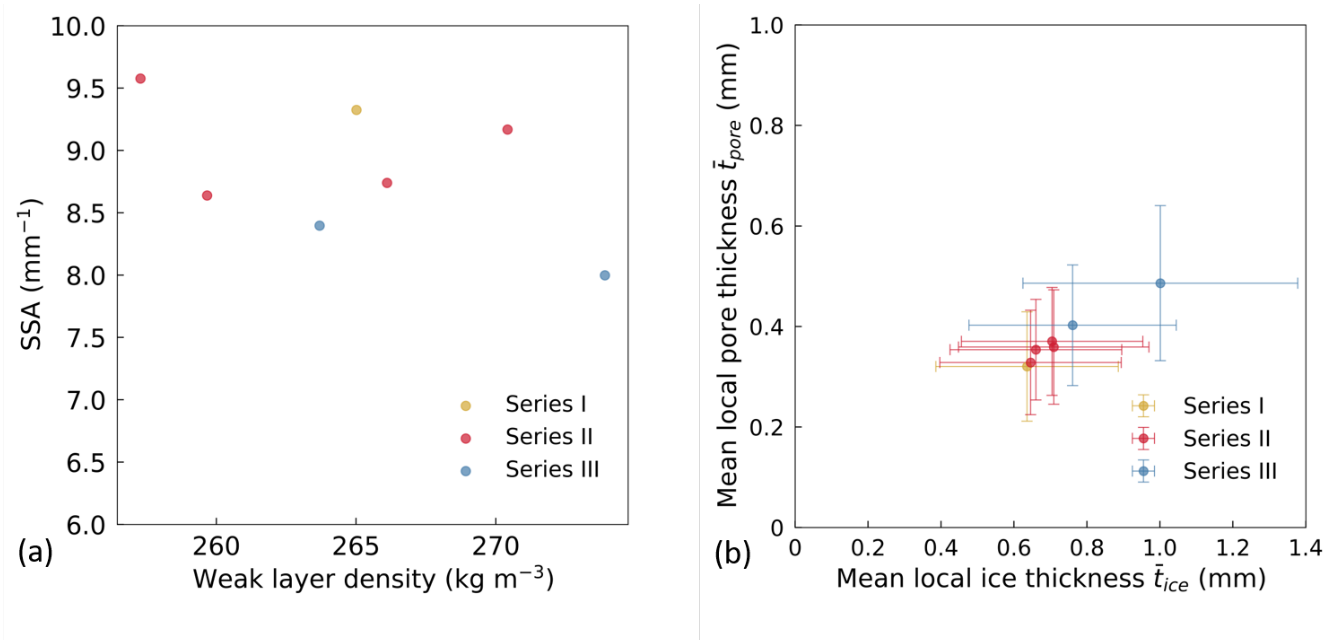

Figure 13. a) Specific surface area (SSA) against weak layer density. b) Local mean pore thickness versus mean ice thickness.

4.1 Fracture toughness and mixed-mode behaviour

We observed that the critical cut length increased with slope angle for downslope cuts (Figure 6), consistent with earlier findings for buried surface hoar (Adam et al., 2024). In contrast, upslope cuts showed only a slight increase in cut length with tilt angle; however, the number of upslope tests was limited. At steep inclines, downslope cuts generally had higher critical cut lengths than upslope cuts, which is in line with theoretical expectations that shear contributions are larger in downslope cuts (Weißgraeber and Rosendahl, 2023). Since the critical cut length marks the onset of crack propagation, it is closely related to fracture toughness, although it is not a material property, rather a system response and depends on cutting direction, slab layering, load and geometry, as also shown by Bergfeld et al. (2025).

Based on the derived elastic properties (Table 2), we converted critical cut lengths into mode I and mode II critical energy release rates (Figure 11). The seasonal increase in both $\mathcal{G}_{\mathrm{Ic}}$ and $\mathcal{G}_{\mathrm{IIc}}$ (Table 3, Figure 12) indicates progressive strengthening of the weak layer over time. Our Mode II values between $0.10 \pm 0.022\ \mathrm{J\,m^{-2}}$ and $1.0 \pm 0.18\ \mathrm{J\,m^{-2}}$ were on the same order of magnitude as the Mode II values for faceted crystals reported by Adam et al. (2026) ranging from $0.08 \pm 0.01\ \mathrm{J\,m^{-2}}$ to $0.16 \pm 0.02\ \mathrm{J\,m^{-2}}$. In that study, the layer of faceted crystals tested was well-consolidated and not a weak layer, but rather a slab layer; densities (331 and 335 $\mathrm{kg\,m^{-3}}$) were higher than those of our weak layers (257 and 273 $\mathrm{kg\,m^{-3}}$). Unlike previous MMFT results for buried surface hoar (Adam et al., 2024), the fitted mode II toughness was not consistently much larger than the mode I toughness. This difference may indicate that the mixed-mode fracture resistance depends on the type of weak layer; however, additional datasets are needed to separate material effects from uncertainty in mode coverage, elastic property

https://doi.org/10.5194/egusphere-2026-3554
Preprint. Discussion started: 4 August 2026

derivation, and sample handling. Fitting the mixed-mode interaction law (Eq. 4) yielded $n = 0.178$ and $m = 0.277$, which indicate a strong interaction between modes and are similar to the parameters reported by Adam et al. (2024) for buried surface hoar ($n = 0.2$, $m = 0.45$). As for other highly porous materials, the appropriate mixed-mode interaction law is not known a priori and must be chosen from phenomenological forms (Marsavina et al., 2014). In this work, we chose to use a power law form as it provides a smooth, closed fracture envelope with independently fitted mode I and mode II toughness values, while acknowledging the existence of other envelope shapes.

4.2 Effect of derived elastic properties on fracture toughness

The derived effective weak layer elastic modulus identified in this study ranged from 0.40 ± 0.05 MPa in Series III to 0.66 ± 0.04 MPa in Series II (Table 2), which is $60 - 164$ % higher than previously used value of 0.25 MPa in fracture mechanical analyses (e.g. Adam et al., 2024). This result was consistent across a wide range of inclines and cut directions, suggesting that the assumed weak layer modulus used in earlier studies may lead to a slight overestimation of the energy release rates. The derived density exponents γ were slightly higher (between 4.61 ± 0.24 for Series III and 4.97 ± 0.24 for Series I) than previously reported values around 4.4 (Gerling et al., 2017; Bergfeld et al., 2023a), resulting in slightly lower elastic moduli for the snow slab, ranging from 16 ± 1 to 41 ± 2 MPa. In our measurement series, the slab temperature as well as the snow surface temperature and air temperature (Figures A6, A7 and A8) were generally slightly (1-5 °C) higher than the temperature values reported by Bergfeld et al. (2023a) which could have had a decreasing effect on the elasticity of the snow slab. The slab elastic moduli obtained from our density exponents γ were comparable to those predicted by the scaling laws found by Schöttner et al. (2026) for faceted crystals (with a power law exponent of 4.6 ± 0.6) and depth hoar (with a power law exponent of 5.1 ± 0.3). Together, these results indicate that the combination of DIC-based displacement measurements and series optimization provides a robust estimate of effective elastic properties, although the absolute accuracy cannot be confirmed without independent validation.

4.3 Microstructural interpretation

The observed seasonal increase in fracture toughness suggests a progressive strengthening of faceted weak layers over time, consistent with previous findings for buried surface hoar (Bergfeld et al., 2023a). The manual snow profiles showed an increase in grain size. Moreover, our limited micro-structural observations (Figure 13) showed a nearly constant weak layer density, a decrease in SSA, and an increase in local ice and pore thickness, suggesting a growth of the bonds between the grains. These observations are qualitatively consistent with a process that could strengthen the weak layer. However, with only four sampling days and no statistical analysis, these observations should be regarded as indicative rather than conclusive.

4.4 Limitations and uncertainties

The mixed-mode fracture experiments represent a compromise between experimental precision and the ability to perform many tests under field conditions. In our case, the setup was not fully rigid, introducing artefacts in the measured displacement fields. Although our processing approach (Figure 4) effectively removed rigid-body motion, it could not correct for rotations or

https://doi.org/10.5194/egusphere-2026-3554
Preprint. Discussion started: 4 August 2026

out-of-plane displacements. A more rigid setup would improve the quality of the displacement data and enable a more precise comparison between model and experiment.

A second limitation is that the elastic properties of the slab and weak layer were identified solely through inverse modeling of the DIC-derived displacements using a series optimization approach (Figure 5). This approach reduces noise and improves robustness but also smooths over variability between individual experiments and may mask true scatter in weak layer properties. Ideally, independent measurements of slab and weak layer moduli would be available so that the inverse derivation step could be omitted and critical energy release rates computed directly. In the absence of such measurements, the absolute values reported in Table 2 likely provide reasonable estimates, while the relative trends between measurement series are considered more robust.

Finally, the microstructural dataset is sparse, consisting of only four sampling days with one or two CT samples each (Figure 13). These data provide valuable temporal snapshots of weak layer evolution but cannot resolve short-term fluctuations or spatial variability. Future studies should combine more frequent CT sampling with mechanical testing to better quantify the relationship between microstructural evolution and fracture properties.

4.5 Implications and outlook

Methodologically, our results demonstrate that DIC-based inverse derivation can be successfully applied even to steep MMFT configurations (Figure 7), providing a basis for extending this approach to other weak layer types. Nevertheless, improvements in setup rigidity, sample handling, and video analysis could further reduce experimental uncertainty and allow a broader range of mode mixities to be explored. Future work should combine more frequent CT sampling with mechanical testing to quantify the relationship between microstructural evolution and fracture toughness. Finally, our results provide benchmark data for mixed-mode fracture parameters of faceted crystals, which can be used to improve process-based models for slab avalanche release and, ultimately, contribute to more reliable snow stability forecasting.

5 Conclusions

We performed 118 mixed-mode fracture tests on a natural faceted-crystal weak layer over three weeks. Video recordings and DIC-derived displacement fields were used to inversely identify weak layer and slab elastic properties, which were then used to calculate mode I and mode II critical energy release rates.

We showed that DIC-based inverse derivation can be applied to inclined MMFT configurations and provides experiment-specific estimates of slab and weak layer elastic properties. The faceted-crystal weak layer showed a pronounced seasonal increase in mixed-mode fracture toughness. Fitted $\mathcal{G}_{\mathrm{Ic}}$ increased from $0.29 \pm 0.042\ \mathrm{J\,m^{-2}}$ to $0.67 \pm 0.06\ \mathrm{J\,m^{-2}}$, while $\mathcal{G}_{\mathrm{IIc}}$ increased from $0.10 \pm 0.022\ \mathrm{J\,m^{-2}}$ to $1.0 \pm 0.18\ \mathrm{J\,m^{-2}}$. The resulting interaction law provides, to our knowledge, the first mixed-mode fracture toughness envelope for a faceted crystal weak layer. As the appropriate form of the interaction law is not yet known for this type of weak layer, we adopted a phenomenological power law envelope from Adam et al. (2024). In contrast to previous results for buried surface hoar reported by Adam et al. (2024), mode II fracture toughness was not consistently much

https://doi.org/10.5194/egusphere-2026-3554
Preprint. Discussion started: 4 August 2026

larger than mode I fracture toughness, suggesting a possible dependence on the type of weak layer. The increase in fracture toughness occurred while weak layer density remained nearly constant, but coincided with decreasing specific surface area and increasing local ice and pore thickness.

These results provide benchmark mixed-mode fracture parameters for weak layers of faceted crystals and demonstrate the value of combining field fracture tests with displacement-based inverse modeling. Future work should combine more frequent, co-located mechanical and microstructural measurements to quantify the link between weak layer microstructure and fracture toughness.

https://doi.org/10.5194/egusphere-2026-3554
Preprint. Discussion started: 4 August 2026

Data availability. The dataset is available on EnviDat at https://doi.org/10.16904/envidat.781. [currently only available upon request - will be published after acceptance.]

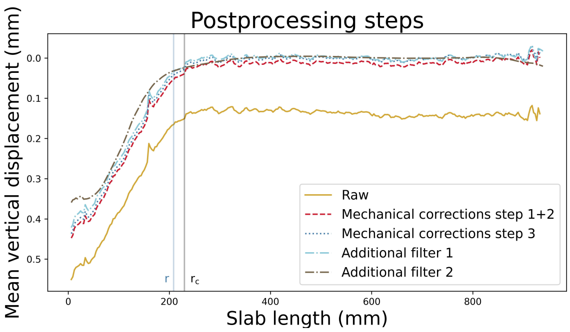

Figure A1. Exemplary mean vertical displacement over slab length for cut length r (blue vertical line) close to critical cut length r_c (black vertical line). Shown are the various filtering steps: the raw displacement (yellow, solid) and the mechanical correction steps 1 (static noise removal) and 2 (correction for sledge motion) (red dashed line). The mechanical correction step 3 (correction for vertical offset) (blue dotted line) was used for further analysis. For comparison, we show the additional filter step 1 with the Savitzky–Golay smoothing (dash-dotted light-blue line) and step 2 with non-local means filtering (dash-dotted brown line) which were not used for further analysis.

https://doi.org/10.5194/egusphere-2026-3554
Preprint. Discussion started: 4 August 2026

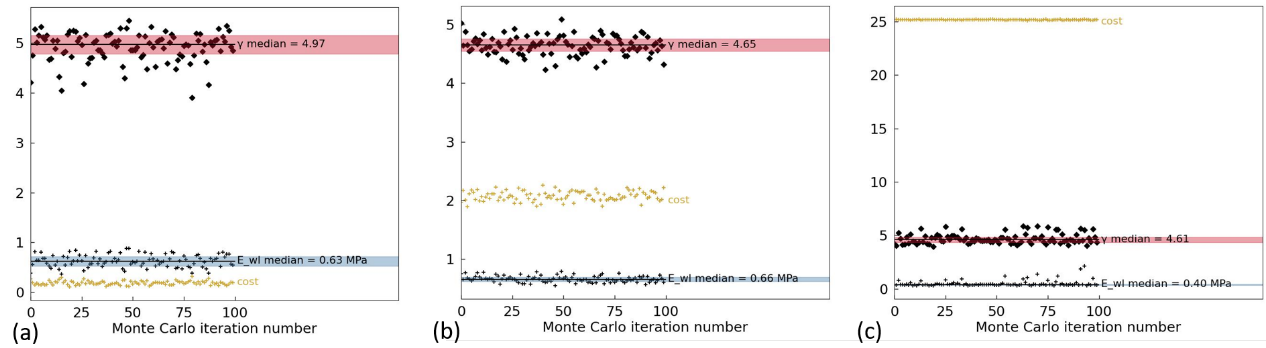

Figure A2. The Monte Carlo sampling results of the series optimization (a) Series I, b) Series II and c) Series III), showing the results for weak layer effective elastic modulus E_{wl} and density parametrization exponent γ for the slab elasticity per Monte Carlo iteration. The solid horizontal lines show the median values and the colored uncertainty ranges are based on the median absolute values. The cost function values (light blue points) were stable across Monte Carlo iterations, with no evidence of systematic drift or spurious convergence.

https://doi.org/10.5194/egusphere-2026-3554
Preprint. Discussion started: 4 August 2026

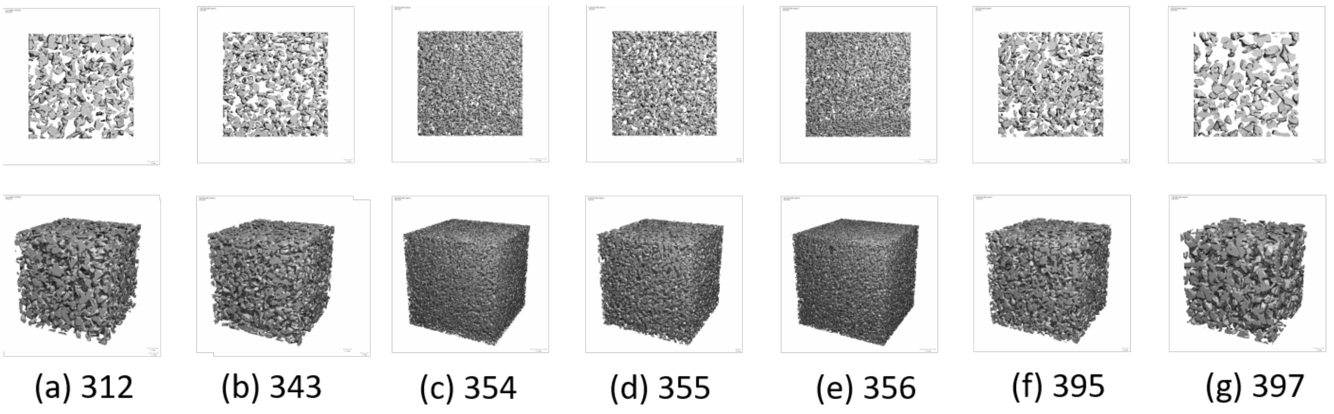

Figure A3. 2D and 3D reconstructed CT images and their ID number. The samples were taken from the field on 14 February 2023 (ID number 312), 28 February 2023 (ID numbers 343 and 354), 2 March 2023 (ID numbers 355 and 356), and 8 March 2023 (ID numbers 395 and 397).

https://doi.org/10.5194/egusphere-2026-3554
Preprint. Discussion started: 4 August 2026

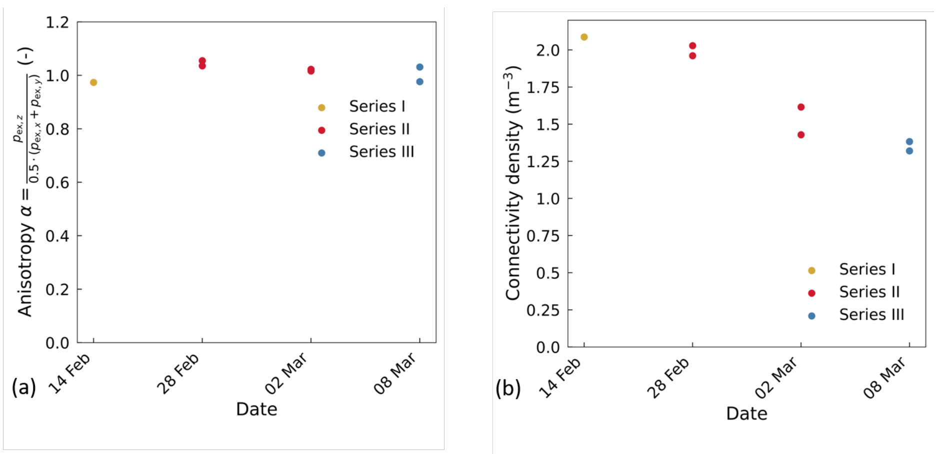

Figure A4. a) Anisotropy and b) connectivity density of the weak layer, as obtained via micro-computed tomography.

https://doi.org/10.5194/egusphere-2026-3554
Preprint. Discussion started: 4 August 2026

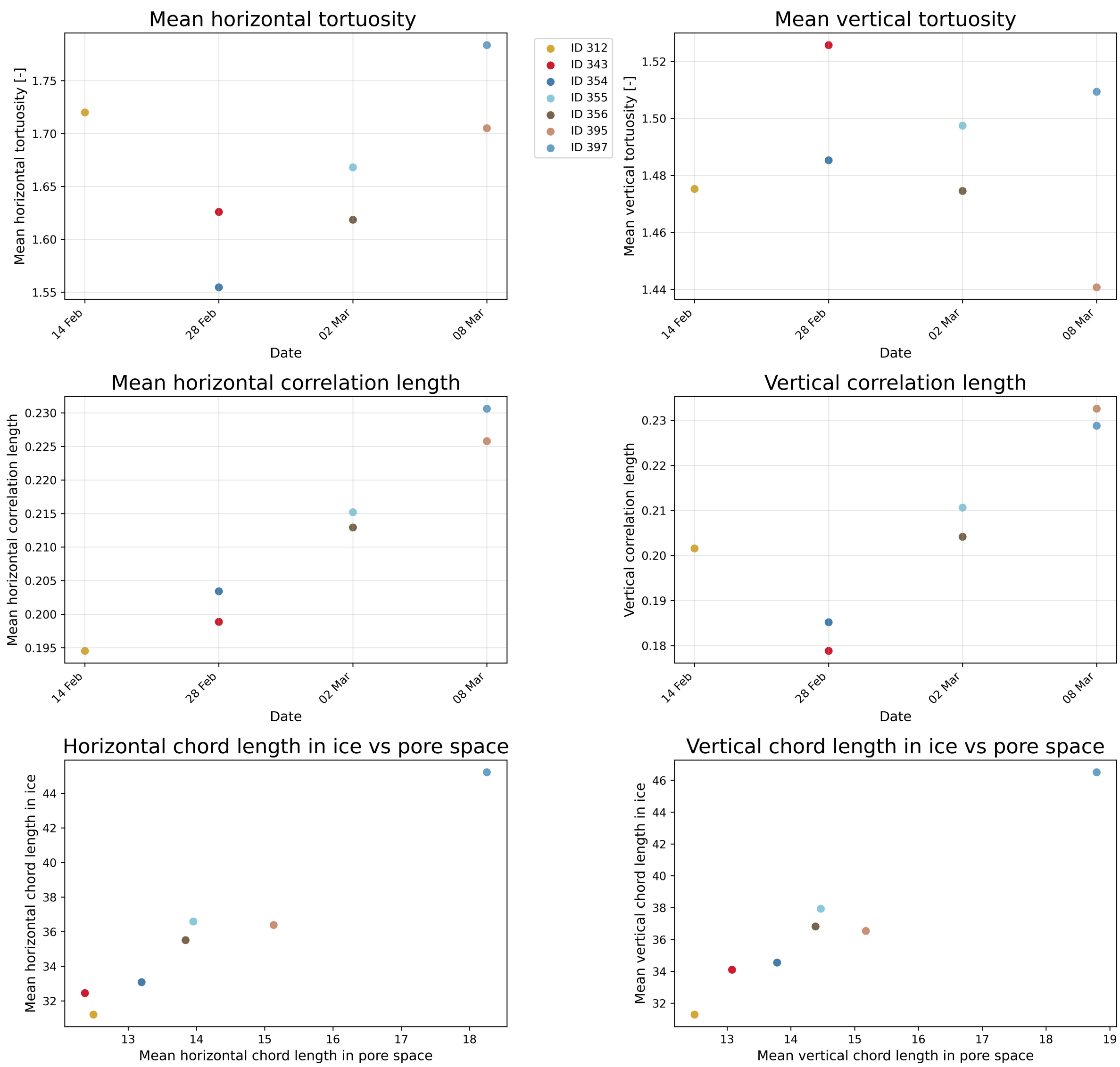

Figure A5. The mean horizontal and vertical tortuosity (top), mean horizontal and vertical correlation lengths (middle) and chord lengths in ice vs pore space (bottom). For each, we show the average of x and y as the horizontal component. Tortuosity seems to increase in the horizontal direction and scatter in the vertical direction. The correlation length increased in horizontal directions, and also in vertical directions, although the first data point (ID 312) is a slight outlier. This similar increase of correlation lengths in all directions is in line with the constant anisotropy as presented in the Results section. The chord length distributions show the statistical lengths of straight lines within a single phase and appear to generally increase in time.

https://doi.org/10.5194/egusphere-2026-3554
Preprint. Discussion started: 4 August 2026

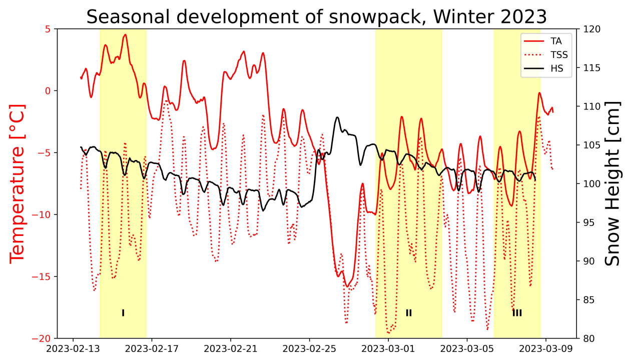

Figure A6. Seasonal development of the snowpack, as measured by weather station WAN7. Displayed are air temperature (red), snow surface temperature (red, dotted), and snow height (black)

https://doi.org/10.5194/egusphere-2026-3554
Preprint. Discussion started: 4 August 2026

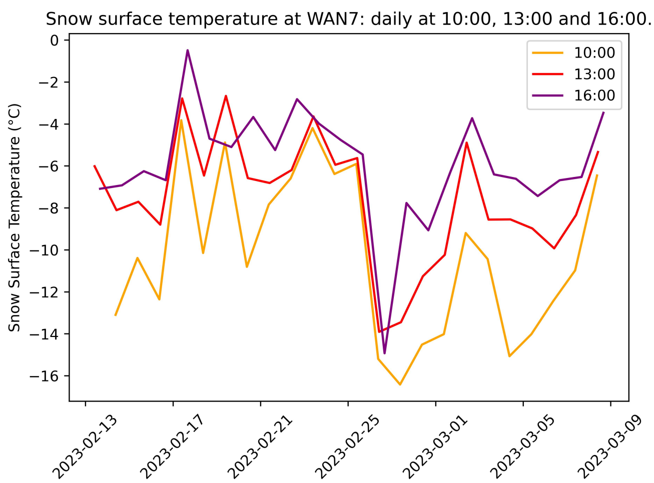

Figure A7. Seasonal development of the snow surface temperature as measured by weather station WAN7: daily values at 10:00, 13:00, and 16:00.

https://doi.org/10.5194/egusphere-2026-3554
Preprint. Discussion started: 4 August 2026

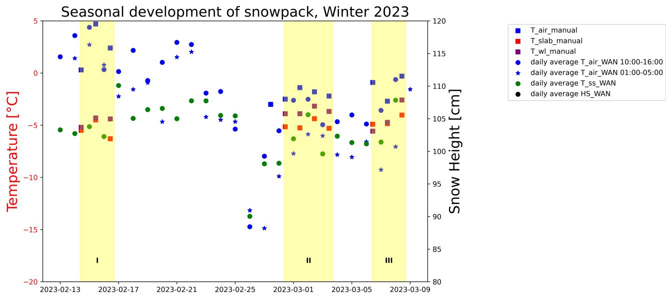

Figure A8. Seasonal development of the air temperature (blue), snow surface temperature (green), slab temperature (red), and weak layer temperature (purple). The manual air temperature was measured at 10:30. For the automatically measured air temperatures, 4-hour averages of day (10:00 to 16:00) and night (01:00 to 05:00) are displayed. All other averages are for the period 10:00 to 16:00, which is also the time period when the measurements were performed.

https://doi.org/10.5194/egusphere-2026-3554
Preprint. Discussion started: 4 August 2026

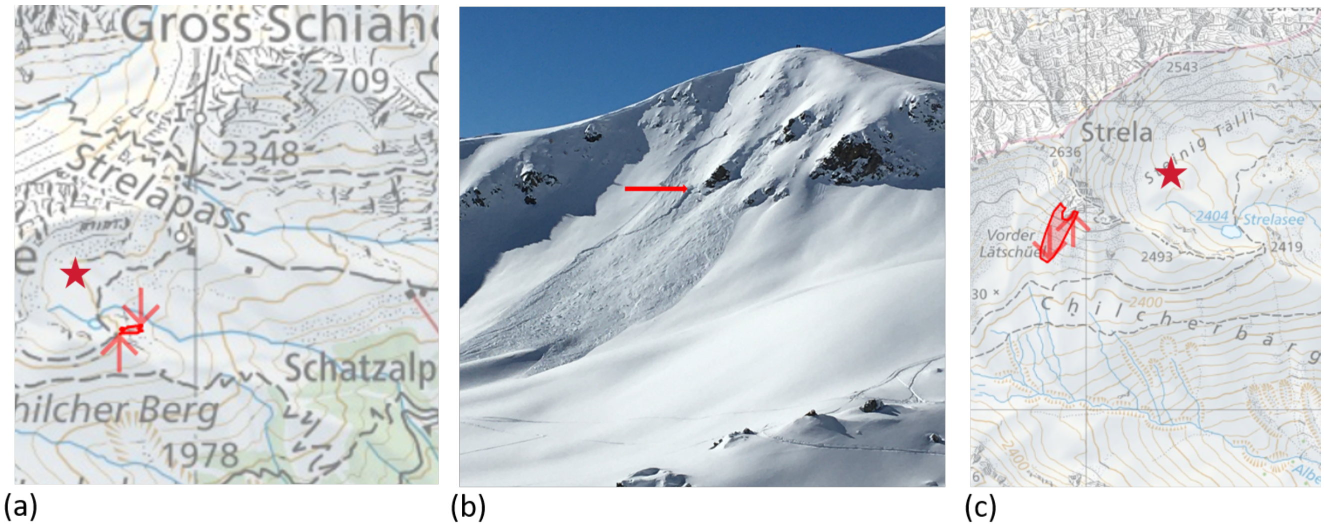

Figure A9. a) Slab avalanche on 7 February 2023 (red arrows), located right below the measurement field (red star), b) Aerial photo of the 7 February 2023 avalanche, which shows that the upper part of the avalanche was caused by a crack in a weak layer higher in the snowpack. In the lower part (highlighted by the red arrow), another crack propagated in a weak layer lower in the snowpack, which is the weak layer we investigated in this manuscript (Picture from SLF Pro, uploaded by Pius Fähndrich). c) Spontaneously released avalanche on the other side of the study site on 14 March 2023 (Info from SLF Pro, uploaded by Mirjam Eberli).

Author contributions. Melin Walet: Conceptualization, Data Curation, Formal analysis, Investigation, Methodology, Software, Validation, Visualization, Writing - original draft, Writing - review & editing. Jakob Schöttner: Conceptualisation, Data Curation, Formal analysis, Investigation, Methodology, Software, Writing - review & editing. Valentin Adam: Conceptualisation, Formal analysis, Investigation, Methodology, Software, Writing - review & editing. Florian Rheinschmidt: Investigation, Methodology, Writing - review & editing. Philipp Rosendahl: Conceptualization, Formal analysis, Funding acquisition, Methodology, Software, Supervision, Validation, Writing review & editing. Philipp Weissgraeber: Conceptualization, Formal analysis, Methodology, Supervision, Writing - review & editing. Jürg Schweizer: Conceptualization, Supervision, Validation, Writing - review & editing. Alec van Herwijnen: Conceptualization, Data Curation, Formal analysis, Investigation, Funding acquisition, Methodology, Project administration, Resources, Software, Supervision, Validation, Writing - review & editing.

Competing interests. At least one of the (co-)authors is a member of the editorial board of The Cryosphere.

https://doi.org/10.5194/egusphere-2026-3554
Preprint. Discussion started: 4 August 2026

Acknowledgements. The authors want to thank the various people who helped out in the field: Bastian Bergfeld, Ivan Calic, Simon Grueter, Mirjam Eberli, Chiara Ghielmini, Michel Geiser, Michael Wuethrich, Michelle Dreifuss, Fabia Unternaehrer and Francis Meloche. Many thanks to Matthias Spieler for the field photography and to Chasper Buchli for the technical support for the weather station. We used Cursor to enhance the efficiency of the inverse modeling code and we used chatgpt.com to enhance the language and readability of this manuscript.

This research has been supported by the Swiss National Science Foundation (SNF) under Grant No. 201071 and by the Deutsche Forschungsgemeinschaft (DFG, German Research Foundation) under Grant No. 460195514.

References

Adam, V., Bergfeld, B., Weißgraeber, P., and et al.: Fracture toughness of mixed-mode anticracks in highly porous materials, Nature Communications, 15, 7379, https://doi.org/https://doi.org/10.1038/s41467-024-51491-7, 2024.

Adam, V., Rheinschmidt, F., Schöttner, J., Walet, M. D., Bergfeld, B., Weißgraeber, P., van Herwijnen, A., and Rosendahl, P. L.: Mixed-mode fracture of porous, bonded snow, Engineering Fracture Mechanics, 343, 112 283, https://doi.org/https://doi.org/10.1016/j.engfracmech.2026.112283, 2026.

Bergfeld, B., van Herwijnen, A., Reuter, B., Bobillier, G., Dual, J., and Schweizer, J.: Dynamic crack propagation in weak snowpack layers: insights from high-resolution, high-speed photography, The Cryosphere, 15, 3539–3553, https://doi.org/10.5194/tc-15-3539-2021, 2021.

Bergfeld, B., van Herwijnen, A., Bobillier, G., Rosendahl, P. L., Weißgraeber, P., Adam, V., Dual, J., and Schweizer, J.: Temporal evolution of crack propagation characteristics in a weak snowpack layer: conditions of crack arrest and sustained propagation, Natural Hazards and Earth System Sciences, 23, 293–315, https://doi.org/10.5194/nhess-23-293-2023, 2023a.

Bergfeld, B., van Herwijnen, A., and Schweizer, J.: Time series data on dynamic crack propagation in long propagation saw tests, EnviDat, https://doi.org/10.16904/envidat.365, 2023b.

Bergfeld, B., Birkeland, K., Adam, V., Rosendahl, P., and van Herwijnen, A.: The effect of propagation saw test geometries on critical cut length, Natural Hazards and Earth System Sciences, 25, 321–334, https://doi.org/10.5194/nhess-25-321-2025, 2025.

Boggs, P. T., Byrd, R. H., and Schnabel, R. B.: A stable and efficient algorithm for nonlinear orthogonal distance regression, SIAM Journal on Scientific and Statistical Computing, 8, 1052–1078, 1987.

Domander, R., Felder, A. A., and Doube, M.: BoneJ2 - Refactoring Established Research Software, Wellcome Open Research, 6, 37, https://doi.org/10.12688/wellcomeopenres.16619.2, 2021.

Doube, M., Kłosowski, M. M., Arganda-Carreras, I., Cordelières, F. P., Dougherty, R. P., Jackson, J. S., Schmid, B., Hutchinson, J. R., and Shefelbine, S. J.: BoneJ: Free and Extensible Bone Image Analysis in ImageJ, Bone, 47, 1076–1079, https://doi.org/10.1016/j.bone.2010.08.023, 2010.

Fierz, C. et al.: The International Classification for Seasonal Snow on the Ground, IHP-VI Technical Documents in hydrology, UNESCO/IHP, 2009.

Gauthier, D. and Jamieson, B.: Towards a field test for fracture propagation propensity in weak snowpack layers, Journal of Glaciology, 52, 164–168, https://doi.org/10.3189/172756506781828962, 2006.

Gerling, B., Löwe, H., and van Herwijnen, A.: Measuring the Elastic Modulus of Snow, Geophysical Research Letters, 44, https://doi.org/10.1002/2017GL075110, 2017.

Heierli, J. and Zaiser, M.: Failure initiation in snow stratifications containing weak layers: Nucleation of whumpfs and slab avalanches, Cold Regions Science and Technology, 52, 385–400, https://doi.org/10.1016/j.coldregions.2007.02.007, 2008.

Marsavina, L., Constantinescu, D., Linul, E., Apostol, D., Voiconi, T., and Sadowski, T.: Refinements on fracture toughness of PUR foams, Engineering Fracture Mechanics, 129, 54–66, https://doi.org/10.1016/j.engfracmech.2013.12.006, 2014.

Mellor, M.: A Review of Basic Snow Mechanics, in: Snow Mechanics Symposium, Proceedings of the Grindelwald Symposium, April 1974, vol. 114 of *IAHS Publication*, pp. 251–291, International Association of Hydrological Sciences, 1975.

Odgaard, A. and Gundersen, H.: Quantification of connectivity in cancellous bone, with special emphasis on 3-D reconstructions, Bone, 14, 173–182, https://doi.org/https://doi.org/10.1016/8756-3282(93)90245-6, 1993.

Roque, W. L. and Costa, R. R.: A plugin for computing the pore/grain network tortuosity of a porous medium from 2D/3D MicroCT image, Applied Computing and Geosciences, 5, 100 019, https://doi.org/https://doi.org/10.1016/j.acags.2020.100019, 2020.

Schindelin, J., Arganda-Carreras, I., Frise, E., Kaynig, V., Longair, M., Pietzsch, T., Preibisch, S., Rueden, C., Saalfeld, S., Schmid, B., Tinevez, J. Y., White, D. J., Hartenstein, V., Eliceiri, K., and Tomancak, P.and Cardona, A.: Fiji: an open-source platform for biological-image analysis., Nature Methods, 9, 676–682, https://doi.org/https://doi.org/10.1038/nmeth.2019, 2012.

Schneebeli, M. and Johnson, J. B.: A constant-speed penetrometer for high-resolution snow stratigraphy, Annals of Glaciology, 26, 107–111, https://doi.org/10.3189/1998AoG26-1-107-111, 1998.

Schneebeli, M. and Sokratov, S.-A.: Tomography of temperature gradient metamorphism of snow and associated changes in heat conductivity, Hydrological Processes, 18, 3655–3665, 2004.

Schneider, C. A., Rasband, W. S., and Eliceiri, K. W.: NIH Image to ImageJ: 25 Years of Image Analysis, Nature Methods, 9, 671–675, https://doi.org/10.1038/nmeth.2089, 2012.

Schweizer, J. and Jamieson, J.: Snow cover properties for skier triggering of avalanches, Cold Regions Science and Technology, 33, 207–221, https://doi.org/10.1016/S0165-232X(01)00039-8, 2001.

Schweizer, J., McCammon, I., and Jamieson, J. B.: Snowpack observations and fracture concepts for skier-triggering of dry-snow slab avalanches, Cold Regions Science and Technology, 51, 112–121, https://doi.org/10.1016/j.coldregions.2007.04.019, 2008.

Schweizer, J., van Herwijnen, A., and Reuter, B.: Measurements of weak layer fracture energy, Cold Regions Science and Technology, 69, 139–144, https://doi.org/10.1016/j.coldregions.2011.06.004, 2011.

Schöttner, J., Zeller-Plumhoff, B., Hagenmuller, P., Weißgraeber, P., Rosendahl, P. L., Löwe, H., Schweizer, J., and van Herwijnen, A.: The influence of snow microstructure on the compressive mechanical properties of weak snowpack layers, Acta Materialia, 302, 121 657, https://doi.org/10.1016/j.actamat.2025.121657, 2026.

Sigrist, C. and Schweizer, J.: Critical energy release rates of weak snowpack layers determined in field experiments, Geophysical Research Letters, 34, https://doi.org/10.1029/2006GL028576, 2007.

Turner, D., Crozier, P., and Reu, P.: Digital image correlation engine, Technical Report - National Technology and Engineering Solutions of Sandia, LLC (NTESS), 2015.

van Herwijnen, A. and Jamieson, B.: Snowpack properties associated with fracture initiation and propagation resulting in skier-triggered dry snow slab avalanches, Cold Regions Science and Technology, 50, 13–22, https://doi.org/10.1016/j.coldregions.2007.02.004, 2007.

van Herwijnen, A., Schweizer, J., and Heierli, J.: Measurement of the deformation field associated with fracture propagation in weak snowpack layers, Journal of Geophysical Research, 115, F03 042, https://doi.org/10.1029/2009JF001515, 2010.

van Herwijnen, A., Gaume, J., Bair, E. H., Reuter, B., Birkeland, K. W., and Schweizer, J.: Estimating the effective elastic modulus and specific fracture energy of snowpack layers from field experiments, Journal of Glaciology, 62, 997–1007, https://doi.org/10.1017/jog.2016.90, 2016.

Weißgraeber, P. and Rosendahl, P. L.: A closed-form model for layered snow slabs, The Cryosphere, 17, 1475–1496, https://doi.org/10.5194/tc-17-1475-2023, 2023.

WSL Institute for Snow and Avalanche Research SLF: Schnee und Lawinen in den Schweizer Alpen: Hydrologisches Jahr 2024/25, 2025.